Flow Computation and Mass Balance in Galerkin Finite-Element Groundwater Models

Emin C. Dogrul, P.E.[1]; and Tariq N. Kadir, P.E.[2]

Abstract: In most groundwater modeling studies, quantification of the flow rates at domain and subdomain boundaries is as important as the computation of the groundwater heads. The computation of these flow rates is not a trivial task when a finite-element method is chosen to solve the groundwater equation. Generally, it is believed that finite-element methods do not conserve mass locally. In this paper, a postprocessing technique is developed to compute mass-conserving flow rates at element faces. It postprocesses the groundwater head field obtained by the Galerkin finite-element method, and the calculated flow rates conserve mass locally and globally. The only requirement for the postprocessor to be applicable is the irrotationality of the flow field, i.e., the curl of the Darcy flux should be zero. The accuracy and the mass conservation properties of the new postprocessor are demonstrated using several test problems that include one-, two-, and three-dimensional flow systems in both homogeneous and heterogeneous aquifer conditions.

DOI: 10.1061/(ASCE)0733-9429(2006)132:11(1206)

CE Database subject headings: Finite element method; Mass; Ground-water flow; Computer analysis; Computation; Hydrologic models.

Introduction

Finite-element methods, particularly the Galerkin finite-element method (GFEM), are commonly utilized in groundwater modeling studies because complex boundaries can be represented more closely. Generally, the momentum equation, i.e., Darcy equation, is substituted into the equation of mass conservation, and the resulting equation is solved for the groundwater head. In most groundwater modeling studies, quantification of flow rates is as important as the simulation of the groundwater heads. One reason for this is that most groundwater basins are divided into political subdomains such as water districts, counties, or states with differing strategies of managing their groundwater resources. Simulation of groundwater flow rates between adjacent subdomains caused by varying management strategies is sometimes the ultimate goal of a modeling study. Another reason is the need to examine the detailed inflow/outflow components at a subdomain level during calibration and verification stages of a modeling study.

When the flow rates are required, the conventional approach is to postprocess the groundwater head field, computed using GFEM, by substituting it into the Darcy equation and obtaining the flux field. Then, the normal component of the Darcy flux is integrated over the domain or subdomain boundary to obtain the flow rates. However, this postprocessing approach has been shown to generate flow rates that violate local as well as global mass balances. Yeh (1981) reported global mass balance errors of up to 30% when the conventional postprocessing method is used. He suggested that the finite-element approach that is used to simulate the groundwater head field also be applied to Darcy equation with the fluxes as the state variables. Although his method produced better results, test problems still showed mass balance errors of 2–9% (Yeh 1981). Commenting on Yeh's work, Lynch (1984) showed that precise global mass balance can be achieved in GFEM by proper treatment of the Dirichlet boundary conditions. He pointed out that the common practice of discarding Galerkin equations—the discrete version of the conservation equation—along Dirichlet boundaries violates the mass balance by requiring that these fluxes be approximated by the conventional postprocessing method. He showed that retaining the Galerkin equation at Dirichlet boundaries as the equation for the flux resulted in precise global mass balance. Similar observations have been made by other researchers (Carey 1982; Carey et al. 1985; Hughes et al. 2000; Berger and Howington 2002; Carey 2002). In fact, the same idea can be used to compute the internal fluxes, i.e., once the groundwater head at an internal node is computed with GFEM, that node can be treated as a Dirichlet boundary and the Galerkin equation at the node can be solved for the flux (Hughes et al. 2000; Carey 2002). Cordes and Kinzelbach (1992) used an alternative postprocessing method where the elements were subdivided into patches and individual fluxes for each patch were computed by assuming that the flow field was irrotational. In their method, triangular and quadrilateral elements were treated separately.

The aim of this paper is to develop and test a postprocessor that uses the groundwater heads computed by GFEM to obtain flow rates across finite-element faces, i.e., normal flux integrated along each of the element faces, that do not violate local and global mass balances. Once flow rates through each of the ele-

[1]Operations Research Specialist III, State of California Dept. of Water Resources, Bay-Delta Office, Modeling Support Branch, 1416 9th St., Room 252A, Sacramento, CA 95814 (corresponding author). E-mail: dogrul@water.ca.gov

[2]Senior Engineer WR, State of California Dept. of Water Resources, Bay-Delta Office, Modeling Support Branch, 1416 9th St., Room 252-09, Sacramento, CA 95814. E-mail: kadir@water.ca.gov

Note. Discussion open until April 1, 2007. Separate discussions must be submitted for individual papers. To extend the closing date by one month, a written request must be filed with the ASCE Managing Editor. The manuscript for this paper was submitted for review and possible publication on March 15, 2005; approved on December 29, 2005. This paper is part of the ***Journal of Hydraulic Engineering***, Vol. 132, No. 11, November 1, 2006. ©ASCE, ISSN 0733-9429/2006/11-1206–1214/$25.00.

ment faces are computed, flow through the boundary of any subdomain can be calculated by summing the flow rates at those faces that define the boundary. The new postprocessor can be viewed as a variation of Cordes and Kinzelbach's (1992) method with a more rigorous treatment of the irrotationality condition. The proposed postprocessor is also different from their method in that the treatment of triangular and quadrilateral elements is unified into a single procedure.

The proposed postprocessor is developed specifically for the depth-integrated groundwater equation. This equation is obtained by assuming that the change in the groundwater head along a vertical line is negligible, and integrating the three-dimensional conservation equation along the vertical axis (Bear 1988). Even though the method is developed and tested for the depth-integrated groundwater equation, the theory behind it is general enough to be applied to any form of the groundwater equation. As will be stated later, the only requirement is the irrotationality of the flow field which physically suggests that the curl of the Darcy flux is zero and that a velocity potential exists (Bear 1988).

Mathematical Development

The depth-integrated conservation equation for groundwater flow can be written as

$$S\frac{\partial h}{\partial t}+\nabla\cdot\mathbf{q}=f \tag{1}$$

where S=storativity (specific yield for an unconfined aquifer and storage coefficient for a confined aquifer) (dimensionless); $h=h(x,y,t)$=groundwater head [L]; $\mathbf{q}=q_x\mathbf{e_x}+q_y\mathbf{e_y}$=depth-integrated Darcy flux, or simply flux, in vector form with $\mathbf{e_x}$ and $\mathbf{e_y}$ being the unit vectors in the x and y lateral directions, respectively [L^2/T]; f=source/sink term [L/T]; $\nabla=(\partial/\partial x)\mathbf{e_x}+(\partial/\partial y)\mathbf{e_y}$=del operator ($1/L$); and t=time [T]. In Eq. (1), $f=f(h,x,y,t)$=general source/sink term that may be a combination of point sources (e.g., pumping and injection wells), distributed sources (e.g., recharge from an overlaying vadose zone); and head dependent sources (e.g., tile drains, stream–groundwater interaction).

Using the Darcy's law, $\mathbf{q}$ can be represented as

$$\mathbf{q}=-T\nabla h \tag{2}$$

and

$$T=K[\min(h,z_u)-z_b] \tag{3}$$

where T=aquifer transmissivity [L^2/T]; $K=K(x,y)$=hydraulic conductivity [L/T]; and z_u and z_b=top and bottom aquifer elevations [L], respectively. Eq. (3) represents transmissivity for both confined and unconfined aquifers.

Integrating Eq. (1) in a weak sense (Allen et al. 1988) for an arbitrary domain Ω, using the Green's theorem and rearranging the resulting expression gives

$$\int_\Gamma -\mathbf{q}\cdot\mathbf{n}v\,d\Gamma=\int_\Gamma \theta v\,d\Gamma=\int_\Omega\left(S\frac{\partial h}{\partial t}v-\mathbf{q}\cdot\nabla v-fv\right)d\Omega \tag{4}$$

where $v=v(x,y)$=an admissible test function; Γ=boundary surrounding the domain Ω; $\mathbf{n}$=outward unit vector perpendicular to Γ; and $\theta=-\mathbf{q}\cdot\mathbf{n}$=flux normal to Γ. Based on the boundary conditions, Γ can be divided into Dirichlet boundary, Γ_D, where groundwater head is specified and Neumann boundary, Γ_N, where normal flux, θ_N, is specified. After expressing the boundary integral in Eq. (4) as the summation of integrals over the Dirichlet and Neumann boundaries and substituting Darcy's law into Eq. (4), the exact normal flux at the Dirichlet boundary, θ_D, satisfies the following equality:

$$\int_{\Gamma_D}\theta_D v\,d\Gamma_D=\int_\Omega\left(S\frac{\partial h}{\partial t}v+T\nabla h\cdot\nabla v-fv\right)d\Omega-\int_{\Gamma_N}\theta_N v\,d\Gamma_N \tag{5}$$

Eq. (5) is the weak formulation of the groundwater conservation equation on which GFEM is based. It should be noted that even though the exact normal flux, θ_D, at the Dirichlet boundary appears in Eq. (5), no information can be deduced as to its functional form. The left-hand side of Eq. (5) actually represents the net flow through the Dirichlet boundary in a weak sense.

In GFEM, a set of basis functions, $\{\omega_i\}$, on a discretization of Ω are used as the test functions, and the head is approximated as (Allen et al. 1988)

$$\tilde{h}=\sum_{i=1}^{m}h_i(t)\omega_i(x,y) \tag{6}$$

where m=number of nodal points based on the discretization. In the remainder of this mathematical development it will be assumed that the basis functions used in Eq. (6) are linear Lagrange basis functions since they are a typical choice in most GFEM applications. Substituting Eq. (6) into Eq. (5) and using the basis functions as the test functions, one can express the flow through a section of the Dirichlet boundary associated with boundary node i, Q_i, as follows:

$$\begin{aligned}Q_i&=\int_{\Gamma_D}\theta_D\omega_i\,d\Gamma_D\\&=\int_\Omega\left(S\omega_i\sum_{j=1}^{m}\frac{\partial h_j}{\partial t}\omega_j+T\sum_{j=1}^{m}h_j\nabla\omega_j\cdot\nabla\omega_i-f\omega_i\right)d\Omega\\&\quad i=1,\ldots,m_D\end{aligned} \tag{7}$$

where m_D=number of boundary nodes that are specified as Dirichlet nodes. Only one type of boundary condition, either Dirichlet or Neumann, can be specified at a node. Since Eq. (7) represents the flux integral at a Dirichlet boundary node, the term that represents the flux integral over the Neumann boundary, Γ_N, does not appear in Eq. (7).

During the application of GFEM, further modifications on Eq. (7) are performed: a mass lumping technique may be applied on the time derivative (Allen et al. 1988); the time derivative may be discretized using finite difference method; transmissivity may be approximated as a piecewise constant over elements, as an expression similar to the one given in Eq. (6) or simply as a constant over the entire domain. Regardless of the specific modifications, Eq. (7) is the expression for groundwater flow at the Dirichlet boundary nodes that is consistent with the GFEM. It is, in fact, the Galerkin equation at the Dirichlet boundary that must be retained as the flow equation (Lynch 1984). During the application of GFEM, the right-hand side of Eq. (7) is evaluated to compute the groundwater heads. The calculation of the flow at the Dirichlet boundary nodes using Eq. (7) requires a small amount of computation time and the mass balance obtained by using these flows is accurate up to the machine precision (Hughes et al. 2000).

Eq. (7) is written for an arbitrary domain, Ω, and its enclosing boundary, Γ. Therefore, it is valid for any collection of elements: the set of all elements that approximate the entire model domain,

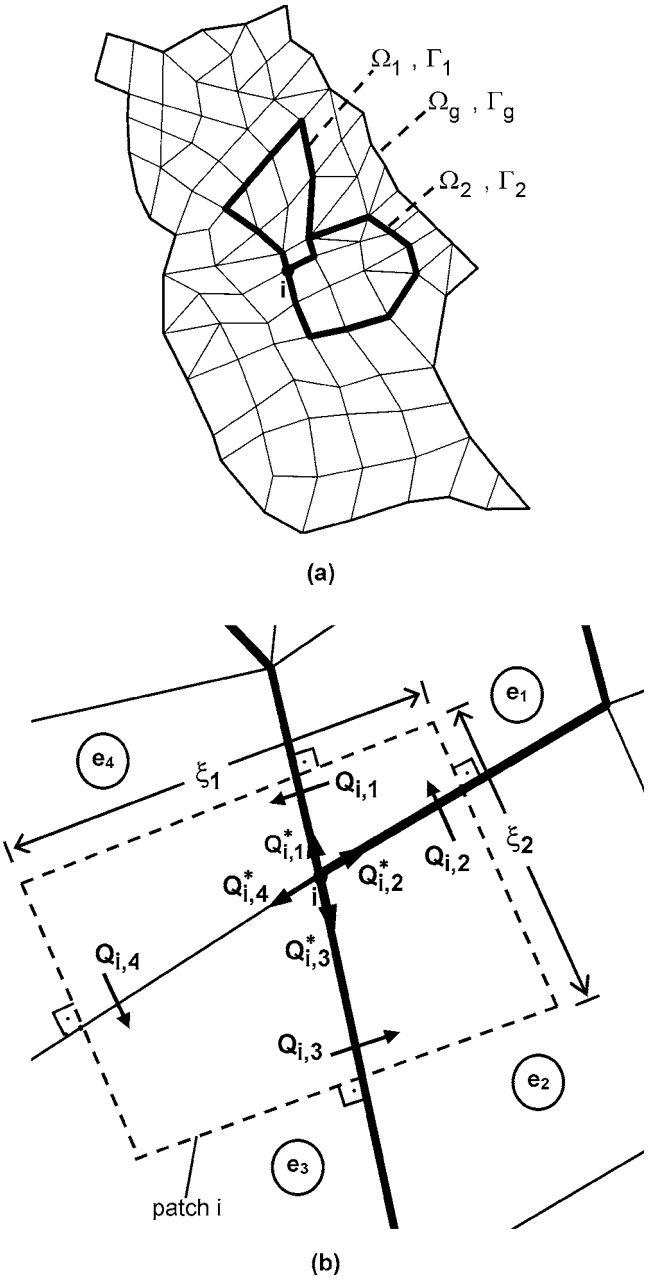

Fig. 1. Descriptive schematics of: (a) discretizations of global domain and two subdomains; (b) enlarged view of vicinity of node i

a subset of these elements or even an individual element. Fig. 1(a) depicts an example discretization of global domain, Ω_g, and two groups of elements that represent subdomains, Ω_1 and Ω_2, and their respective enclosing boundaries Γ_g, Γ_1, and Γ_2. When Eq. (7) is written for any of the subdomains, the head values at the subdomain boundary nodes that are obtained from the application of GFEM can be treated as Dirichlet boundary nodes. Then, Eq. (7) produces the flows at the boundary nodes of the subdomains Ω_1 and Ω_2. As such, Eq. (7) is a postprocessing technique for the recovery of the boundary flows based on the nodal head values and it is consistent with the GFEM approximation.

The aim of this paper is to utilize Eq. (7) to compute flows through each of the element faces of the finite-element grid so that a precise mass balance for arbitrarily defined collections of elements as well as the flows between adjacent element collections can be computed. To achieve this, however, Eq. (7) alone cannot be used and it is necessary to utilize further information such as the irrotationality of the flow field. To demonstrate this point, node i in Fig. 1(a), which lies between two subdomains, will be considered. Fig. 1(b) shows an enlarged view of the vicinity of node i and the corresponding patch with e_1 and e_2 as the elements that belong to subdomains 1 and 2, respectively. Patch i in Fig. 1(b) is constructed by connecting the lines that perpendicularly cross element faces at midpoints. When Eq. (7) is written for element e_1 at node i, it represents the flow through the section of the element boundary that is associated with node i [i.e., the section that extends from the midpoint of the element face on one side of node i to the midpoint of the face on the other side of the node, see Fig. 1(b)]

$$Q_i^{e_1} = \int_{\Omega^{e_1}} F_i \, d\Omega^{e_1} = Q_{i,2} - Q_{i,1} \tag{8}$$

where Q_i^{e1}=net flow that crosses the section of the boundary of element e_1 associated with node i; F_i=integrand in Eq. (7); Ω^{e_1}=domain of element e_1; $Q_{i,1}$=flow through half of the interface between elements e_1 and e_4; and $Q_{i,2}$=flow through half of the interface between elements e_1 and e_2, as depicted in Fig. 1(b). The domain of the integral in Eq. (8) is taken to be the domain of element e_1, Ω^{e_1}, to be consistent with the GFEM where the integrals are evaluated over individual elements. Since the exact normal flux expressed as a function of distance along the faces of element e_1 is not known, $Q_{i,1}$ and $Q_{i,2}$ cannot be determined directly; Eq. (8) represents a single equation with two unknowns. Writing Eq. (7) also for element e_2 at node i produces two equations with three unknowns, namely $Q_{i,1}$, $Q_{i,2}$, and $Q_{i,3}$. Finally, expressing Eq. (7) for all the surrounding elements of node i generates four equations with four unknowns but the resulting system of equations is underdetermined, i.e., one of the equations in the system is a linear combination of the rest

$$\begin{bmatrix} -1 & 1 & 0 & 0 \\ 0 & -1 & 1 & 0 \\ 0 & 0 & -1 & 1 \\ 1 & 0 & 0 & -1 \end{bmatrix} \begin{Bmatrix} Q_{i,1} \\ Q_{i,2} \\ Q_{i,3} \\ Q_{i,4} \end{Bmatrix} = \begin{Bmatrix} Q_i^{e_1} \\ Q_i^{e_2} \\ Q_i^{e_3} \\ Q_i^{e_4} \end{Bmatrix} \tag{9}$$

To close the system of equations, irrotationality of the flow field will be assumed. Similar approaches have also been taken by Cordes and Kinzelbach (1992), and Chou et al. (2004). The irrotationality of the flow field can be expressed as

$$\nabla \times \mathbf{q} = \frac{\partial q_y}{\partial x} - \frac{\partial q_x}{\partial y} = \nabla \cdot \mathbf{q}^* = 0 \tag{10}$$

where $\mathbf{q}^* = q_y \mathbf{e_x} - q_x \mathbf{e_y}$. Writing Eq. (10) in a weak sense using the basis functions and applying the Green's theorem gives

$$Q_i^* = \int_\Gamma \mathbf{q}^* \cdot \mathbf{n} \omega_i d\Gamma = \int_\Omega T \sum_{j=1}^{m} (h_j \nabla^* \omega_i \cdot \nabla \omega_j) d\Omega \quad i = 1, \ldots, m \tag{11}$$

where Q_i^*=circulation at node i (Bear 1988) and $\nabla^* = (\partial/\partial y)\mathbf{e_x} - (\partial/\partial x)\mathbf{e_y}$. Since $\mathbf{q}^* \cdot \mathbf{n} = \mathbf{q} \cdot \mathbf{n_T}$, where $\mathbf{n_T}$=unit tangent at the boundary in a counterclockwise direction, Eq. (11) represents the line integral of the tangential flux at the boundary, Γ. The evaluation of Eq. (11) requires the additional computation of the integral

$$\int_{\Omega} \nabla^* \omega_i \cdot \nabla \omega_j d\Omega \quad i,j=1,\ldots,m \tag{12}$$

where it is assumed that the transmissity is approximated so that it can be taken out of the integral. Regardless of the approximation of the transmissivity, the integral in Eq. (12), or any variants of it due to a particular approximation, needs to be computed only once at the beginning of the simulation.

Adopting the convention where the counterclockwise direction is positive and writing Eq. (11) for element e_1 at node i [Fig. 1(b)] gives

$$Q_i^{*,e_1} = \int_{\Omega^{e_1}} G_i \, d\Omega^{e_1} = Q_{i,2}^* - Q_{i,1}^* \tag{13}$$

where Q_i^{*,e_1}=integral of the tangential flux along the part of the patch boundary that lies in element e_1 [Fig. 1(b)]; G_i=integrand in Eq. (11); $Q_{i,2}^*$=integral of the tangential flux along half of the interface between elements e_1 and e_2; and $Q_{i,1}^*$=integral of the tangential flux along half of the interface between elements e_1 and e_4. Similar to Eq. (8), the domain of the integral in Eq. (13) is taken to be the domain of element e_1 to be consistent with the GFEM. Since the circulation about any closed curve at any location in an irrotational flow has to be zero (Bear 1988), Q_i^{*,e_1} counterbalances the integral of the tangential flux along the faces of element e_1 that fall in patch i, i.e., $Q_{i,2}^* - Q_{i,1}^*$. When Eq. (11) is written at internal nodes, the basis functions vanish at the global boundary and Q_i^* becomes zero. This result is consistent with the theory that the circulation about a closed curve in an irrotational flow is zero. On the other hand, a closed curve around a boundary node cannot be specified, and expressing Eq. (11) at a boundary node produces a nonzero value.

To utilize Eq. (11) as a closure to the system of equations listed in Eq. (9), it is necessary to express the components of the circulation, $Q_{i,k}^*$, in the patch in terms of the flow terms, $Q_{i,k}$. For this purpose, it will be assumed that the normal flux at the element face that falls in the patch is constant and $Q_{i,k}$ can be expressed in terms of this normal flux. For instance, $Q_{i,1}$ in Fig. 1(b) can be used to express the constant normal flux at the half of the interface between elements e_1 and e_4

$$Q_{i,1} = \int_{\Gamma_{e_1,e_4}} \theta \omega_i \, d\Gamma \cong \theta_{e_1,e_4}^i \int_{\Gamma_{e_1,e_4}} \omega_i \, d\Gamma = \theta_{e_1,e_4}^i \frac{L_{e_1,e_4}}{2} \tag{14}$$

or

$$\theta_{e_1,e_4}^i = \frac{2}{L_{e_1,e_4}} Q_{i,1} \tag{15}$$

where θ_{e_1,e_4}^i=constant patch flux normal to the element face that falls into patch i; Γ_{e_1,e_4}=entire interface between the two elements; and L_{e_1,e_4}=total length of the interface. As noted earlier, Eq. (15) is obtained assuming that the linear Lagrange basis is used for ω_i. A similar expression can be written for the normal flux at the interface between elements e_1 and e_2 that falls into patch i [Fig. 1(b)]

$$\theta_{e_1,e_2}^i = \frac{2}{L_{e_1,e_2}} Q_{i,2} \tag{16}$$

Next, it will be assumed that the patch flux normal to the element face is equal to the flux that is tangent to the patch boundary, and it is spatially constant along the corresponding side of the patch. For example, in Fig. 1(b) θ_{e_1,e_4}^i is assumed to be the flux tangent to the side of the patch with length ξ_1. Similarly, θ_{e_1,e_2}^i is assumed to be the flux tangent to the side of the patch with length ξ_2 [Fig. 1(b)]. Finally, using the expressions for the tangent fluxes the irrotationality at an internal node can be written as

$$\sum_{k=1}^{c_i} \frac{2\xi_k}{L_{i,k}} Q_{i,k} = 0 \tag{17}$$

where c_i=number of element faces that connect at node i; $L_{i,k}$=length of the element face k; and ξ_k=length of the patch boundary that crosses element face k perpendicularly. Eq. (17) corresponds to Eq. (11) where the tangent fluxes are approximated in terms of normal fluxes, as described above.

For a boundary node a closed curve cannot be specified and application of Eqs. (11) and (17) generates a nonzero value

$$\sum_{k=1}^{c_i} \frac{2\xi_k}{L_{i,k}} Q_{i,k} = \int_{\Omega} T \sum_{j=1}^{m} (h_j \vec{\nabla}^* \omega_i \cdot \vec{\nabla} \omega_j) d\Omega \tag{18}$$

The right-hand side of Eq. (18) can be computed by using the head and transmissivity values obtained by solving Eq. (1) using GFEM.

Replacing the last equation of the system described in Eq. (9) by Eqs. (17) and (18) for internal and boundary nodes, respectively, produces a well-posed set of equations that can be solved very efficiently. The system of equations is defined for each node and can be solved locally independent from the equation systems defined for other nodes. For an element face identified with nodes i and j, two flow terms will be computed: one for node i that crosses through half of the element face located in patch i, and the other for node j that crosses the other half of the face located in patch j. Once the two flow terms are computed they can be summed to obtain the net flow through the entire element face defined by nodes i and j. The above procedure is applicable when either triangular or quadrilateral or both types of elements are used to discretize the domain.

The preceding mathematical development assumes that the flow is irrotational. It can be shown that the depth-integrated conservation Eq. (1) always satisfies the irrotationality condition (Bear 1988). Therefore, utilizing the above approach can be used under any circumstances as long as Eq. (1) is used to model the groundwater flow.

Verification

The mass-conserving aspect and the accuracy of the proposed postprocessor [i.e., system of Eqs. (9) with the last equation replaced by Eqs. (17) and (18) for internal or boundary nodes, respectively] are demonstrated by comparing the simulated flow rates to their exact counterparts for several test problems. Integrated water flow model (IWFM), a quasi three-dimensional finite-element groundwater model maintained by the State of California Department of Water Resources (CADWR 2005), was used in these test problems.

Example 1

The first example is a one-dimensional problem which deals with the radial flow to a well that fully penetrates a confined aquifer with a uniform thickness of 100 m. The aquifer is homogeneous, isotropic, and has an infinite extent. The hydraulic conductivity

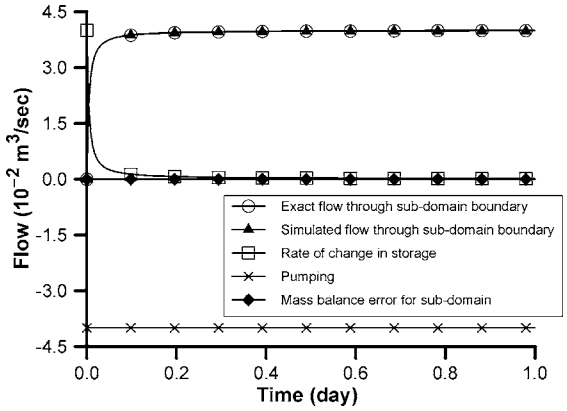

Fig. 2. Mass balance for subdomain with 60 m radius in Example 1

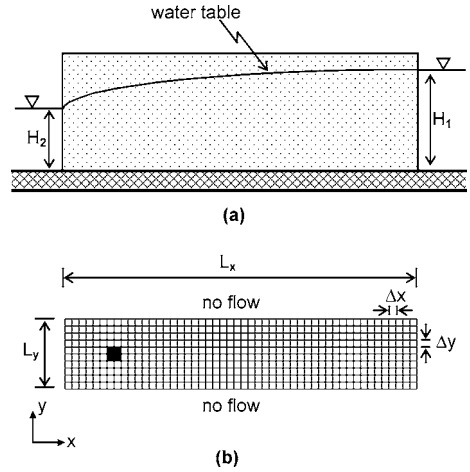

Fig. 3. Definition sketch for Example 2: (a) cross section of heterogeneous aquifer between two lakes; (b) simulation grid (shaded area represents test subdomain)

and the specific storage of the aquifer are 2.3×10^{-5} m/s and 7.5×10^{-6} m^{-1}, respectively. The well diameter is small and the storage in the wellbore can be neglected. The pumping rate is constant at 0.04 m^3/s. The exact expression for the flow at a distance from the well can be obtained by substituting the groundwater head computed by the Theis method (Theis 1935) into the Darcy equation.

Because of its symmetric nature, the system was simulated only in a single quadrant of the domain using nonuniform grid spacing. For purposes of numerical simulation the infinite extent of the aquifer was approximated by setting specified head boundary conditions at 20,000 m away from the well. In the angular direction the quadrant was discretized into eight equal regions. The grid spacing in the radial direction was increased at specified intervals as the distance from the well increased. For distances of 0–200, 200–2,000, and 2,000–20,000 m from the well, the grid spacing was 10, 100, and 1,000 m, respectively. The initial groundwater head and the specified head at the boundary were each set to 150 m (i.e., artesian conditions). The simulation period was 1 day with 10 s time steps. To demonstrate the ability of the proposed postprocessor to conserve mass locally, a circular subdomain with 60 m radius around the well was defined, and the flow terms that were used in checking the local mass balance were simulated. Since the system was simulated only in a single quadrant of the domain, the results were multiplied by 4 to obtain the final flow values.

Fig. 2 shows the rate of change in storage, and inflow and outflow components at the subdomain as well as the mass balance error. For a mass conserving method, the sum of the rate of change in storage and the flow through the circular boundary of the subdomain (located at a 60 m radius from the well) less the pumping rate should be zero. The simulated flow rate through the subdomain boundary shown in Fig. 2 is computed using the proposed postprocessor. Inflows are shown as positive and outflows are shown as negative values. It can be seen in Fig. 2 that the mass balance error for the subdomain is essentially zero for the entire simulation period demonstrating local mass conservation. That is, flow rates computed by the proposed postprocessor satisfy the local mass balance.

For a visual inspection, the exact flow rate through the subdomain boundary is also depicted in Fig. 2. As can be seen, the difference between the exact and the simulated flow rates at the subdomain boundary is undetectable.

Example 2

It has been reported in the literature that as the hydraulic conductivity varies from one element to the next, the local mass balance errors in the GFEM become more prominent. The second example was designed to test the performance of the proposed postprocessor in heterogeneous aquifer conditions in one-, two-, and three-dimensional flow systems. The cross section and the plan view for this example are shown in Figs. 3(a and b), respectively. An unconfined aquifer lies between two lakes. The length of the aquifer in the x direction, L_x, is 10 km and in the y direction, L_y, is 2 km. The surface elevations of the lakes are constant but different from each other. The east and west side lake elevations are H_1=200 m and H_2=150 m, respectively [Fig. 3(a)]. There is no flow across the north and south sides of the aquifer [Fig. 3(b)]. The specific yield, S, of the aquifer is 0.25. The finite-element grid used in the simulation is shown in Fig. 3(b). The grid sizes in x- and y-directions, Δx and Δy, respectively, are both 200 m. The dark region that is comprised of four elements in Fig. 3(b) is the subdomain for which the mass-conserving property of the proposed postprocessor is tested. To simulate heterogeneous aquifer conditions, each element was assigned a random hydraulic conductivity, K. The randomly heterogeneous hydraulic conductivity field, hereafter referred to as the "K field," was assumed lognormally distributed, uncorrelated, and characterized by its coefficient of variation, ρ_K, defined as

$$\rho_K = \frac{\sigma_K}{\bar{K}} \tag{19}$$

where σ_K and $\bar{K}$=standard deviation and the mean of the random K field, respectively. For all test problems $\bar{K}$ was taken to be 100 m/day. Although an uncorrelated K field may result in an unrealistic flow field, the goal is to analyze the accuracy and the mass-conserving property of the proposed postprocessor when hydraulic conductivity varies from one element to the next from a numerical perspective. The results of this analysis should be valid under any type of heterogeneity and flow conditions. Similar studies with uncorrelated K fields have also been reported in the literature (e.g., Durlofsky 1994).

Table 1. Inflow and Outflow Rates Computed by Analytic and Proposed Postprocessor at Domain and Subdomain Boundaries at Different Levels of Heterogeneity; Outflow Rates Are Shown in Parentheses

ρ_K	Analytic (m^3/day)	Postprocessor (m^3/day)	Error (%)	Mass balance error in postprocessor (%)
Entire domain				
0.0	175,000.0 (175,000.0)	175,000.0 (175,000.0)	0.0	0.0
0.5	151,137.2 (151,137.2)	156,092.6 (156,092.6)	3.3	0.0
1.0	105,068.8 (105,068.8)	114,119.7 (114,119.7)	8.6	0.0
2.0	46,887.1 (46,887.1)	54,753.1 (54,753.1)	16.8	0.0
3.0	24,077.0 (24,077.0)	29,668.3 (29,668.3)	23.2	0.0
Subdomain				
0.0	35,000.0 (35,000.0)	35,000.0 (35,000.0)	0.0	0.0
0.5	30,227.4 (30,227.4)	31,218.5 (31,218.5)	3.3	0.0
1.0	21,013.8 (21,013.8)	22,821.9 (22,821.9)	8.6	0.0
2.0	9,377.4 (9,377.4)	10,950.6 (10,950.6)	16.8	0.0
3.0	4,815.4 (4,815.4)	5,933.7 (5,933.7)	23.2	0.0

One-Dimensional Problem

For this problem, the aquifer was assumed to be heterogeneous only in the x direction; i.e., the hydraulic conductivity was varied for each element in the x direction, but no variation was considered in the y direction. Since the north and south boundary conditions are symmetric [Fig. 3(b)], the flow between the two lakes in this case is essentially one dimensional. The exact expression for the flux at the steady state of this problem can be expressed as

$$q = \frac{H_2^2 - H_1^2}{2\Delta x \sum_{i=1}^{ns} \frac{1}{K_i}} \tag{20}$$

where Δx=200 m=grid spacing in x direction; ns=50=number of elements in the x direction; and K_i=realization of the random K field assigned to the ith element. H_1 and H_2=specified head boundary conditions as defined earlier [Fig. 3(a)]. The performance of the proposed postprocessor to compute the element face flows and maintain local and global mass balances was tested for several degrees of heterogeneity with ρ_K taken as 0.0 (homogeneous case), 0.5, 1.0, 2.0, and 3.0.

Table 1 shows the inflow and outflow rates at the boundaries of the entire domain and the subdomain computed by the analytic expression (20) and the proposed postprocessor. The subdomain used in this problem is depicted as the black region comprised of four elements in Fig. 3(b). The deviations of the flow rates computed by the proposed postprocessor from the analytic solutions are also listed in Table 1 as % errors. The last column lists the mass balance error generated by the proposed postprocessor.

The mass balance error in the proposed postprocessor is zero at all levels of heterogeneity both for the entire domain and the subdomain; i.e., the inflow and outflow rates are equal and the mass is conserved at both global and local scales (Table 1). On the other hand, the difference between the flow rates computed analytically and by the proposed postprocessor increases as the heterogeneity increases. This behavior can be attributed to the accuracy of the simulated groundwater heads with respect to the level of heterogeneity. The accuracy of the flow rates can be, at best, as good as the accuracy of the simulated heads since they are computed by postprocessing the head values. Fig. 4 shows the logarithm of the RMS of the normalized head error vector and the normalized error for the simulated inflow rates for the subdomain, versus the level of heterogeneity. Note that the error values for the inflow and outflow rates at the boundary of the entire domain are the same as those at the boundary of the subdomain (Table 1). Therefore, only the flow errors at the subdomain level are considered in the following analysis. The RMS of the normalized head error vector is defined as

$$\text{RMS} = \sqrt{\frac{1}{ns}\sum_{i=1}^{ni}\left(\frac{h_{a_i} - h_{s_i}}{h_{a_i}}\right)^2} \tag{21}$$

where ni=total number of nodes; h_{a_i}=analytic head solution at the ith node; and h_{s_i}=head at the ith node simulated by the GFEM. The normalized flow error is defined as the ratio of the difference between the simulated and the analytic flow to the analytic value. It can be seen in Fig. 4 that the error in the simulated flow almost parallels the error in the simulated head, although the flow error is about 1.5 orders of magnitude larger than the error in head.

The degradation of the accuracy of the simulated heads, and consequently the accuracy of the postprocessed flow rates, at a fixed grid resolution as the heterogeneity increases is common to all numerical methods. The increase in the heterogeneity increases the local head gradients, decreasing the accuracy of the simulated heads when the grid resolution is coarse. For instance, in the current example the maximum head gradient at ρ_K=3.0 is

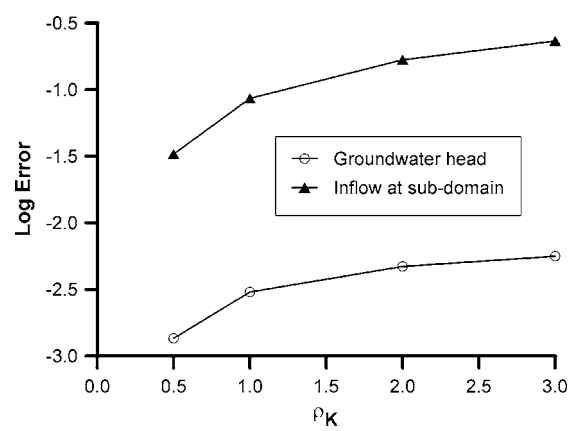

Fig. 4. Comparison of errors in simulated head and postprocessed flow rate at different levels of heterogeneity

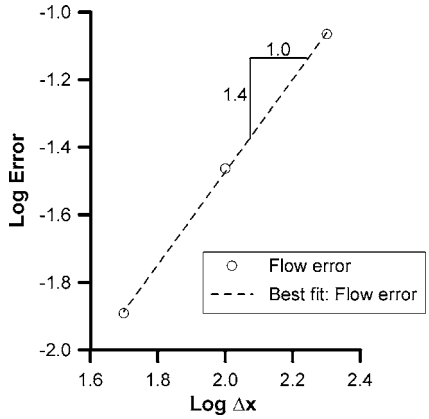

Fig. 5. Log–log plot of flow error versus grid size for $\rho_K=1.0$

6.6 times larger than the maximum head gradient at $\rho_K=0.5$ [the maximum head gradient actually occurs where the subdomain is located; see Fig. 3(b)]. It is a common practice in numerical studies to increase the grid resolution where large head gradients are expected to obtain more accurate simulation results. This practice is based on the fact that the results of a consistent numerical method will converge to the exact solution with a rate equal to the order of accuracy of the numerical method as the grid resolution is refined (Allen et al. 1988).

In the light of the above discussion, the initial grid resolution was refined progressively by halving the grid spacing both in x and y directions, and the flow rates were computed using the proposed postprocessor for $\rho_K=1.0$ to check the order of accuracy of the postprocessor. Fig. 5 shows the logarithm of the grid size versus the logarithm of the normalized inflow error at the subdomain boundary at three grid resolutions (200, 100, and 50 m) along with the least-squares regression line that fits the computed error values best. The order of accuracy of the postprocessor can be estimated by the slope of the regression line, i.e., (log error)/(log Δx). Fig. 5 suggests that the proposed postprocessor to compute element face flows has an order of accuracy of around 1.4. This means that the grid can be refined at parts of the domain where more accurate flow rates are required. The decrease in the error (i.e., difference between the exact and the simulated flow rates) will be proportional to $(\Delta x_c/\Delta x_f)^{1.4}$, where Δx_c and Δx_f=initial and refined grid resolutions, respectively. In a groundwater modeling study, anticipating that highly heterogeneous aquifer conditions are likely to lead to less accurate flow rates, one can increase the grid resolution at highly heterogeneous locations of the domain. For instance, based on the % error values listed in Table 1, a grid resolution of approximately 50 m, compared to 200 m, would be required in the case of $\rho_K=3.0$ to achieve flow rate accuracy similar to that of $\rho_K=0.5$.

Two-Dimensional Problem

For this problem, each element shown in Fig. 3(b) was assigned a realization of the uncorrelated K field with $\rho_K=3.0$. The heterogeneity in both x and y directions led to the two dimensionality of the flow field. The analytical solution cannot be obtained for this problem. Therefore, MODFLOW, a three-dimensional finite difference groundwater model (McDonald and Harbaugh 1988), at a high grid resolution was used to approximate the exact flow rates to be compared to those obtained by the proposed postprocessor. The finite difference mesh used with MODFLOW was refined until the change between the flow rates computed at two successively refined mesh systems was negligible. This was achieved at 6.25 m finite difference grid spacing where the flow rates at the domain and subdomain levels changed 0.3 and 0.5%, respectively, compared to the flow rates computed at 12.5 m grid spacing. In the rest of this document, the exact solutions approximated by MODFLOW will simply be referred to as "exact solutions." Table 2 shows the inflow and outflow rates at the domain and subdomain boundaries computed by the proposed postprocessor compared with the exact counterparts at different grid resolutions. The last column of Table 2 shows that the postprocessor conserves mass both at domain and subdomain levels. It is also apparent that the % error in flow rates decreases as the finite-element mesh is refined [see Error (%) columns in Table 2]. It can be shown that the order of accuracy of the proposed postprocessor is 1.5 and 1.4 when computed based on the error (%) values listed in Table 2 for the entire domain and the subdomain, respectively. These results are consistent with the findings of the one-dimensional problem.

Three-Dimensional Problem

For this problem, the aquifer shown in Fig. 3(a) was discretized into three 70-m-thick layers in the vertical direction. All three layers were discretized laterally using the finite-element mesh shown in Fig. 3(b). An initial grid resolution of $\Delta x=\Delta y=200$ m

Table 2. Comparison of Inflow and Outflow Rates Computed by Proposed Postprocessor to Exact Values at Domain and Subdomain Levels at Different Grid Resolutions when $\rho_K=3.0$; Outflow Rates Are in Parentheses

Δ_x (m)	Exact (m^3/day)	Postprocessor (m^3/day)	Error (%)	Mass balance error in postprocessor (%)
Entire domain				
200	96,723.3 (96,723.3)	117,794.7 (117,794.7)	21.8	0.0
100	96,723.3 (96,723.3)	105,114.5 (105,114.5)	8.7	0.0
50	96,723.3 (96,723.3)	99,730.9 (99,730.8)	3.1	0.0
25	96,723.3 (96,723.3)	97,697.0 (97,697.0)	1.0	0.0
Subdomain				
200	19,407.8 (19,407.8)	25,061.1 (25,061.1)	29.1	0.0
100	19,407.8 (19,407.8)	21,833.3 (21,833.3)	12.5	0.0
50	19,407.8 (19,407.8)	20,346.3 (20,346.3)	4.8	0.0
25	19,407.8 (19,407.8)	19,727.3 (19,727.3)	1.7	0.0

Table 3. Comparison of Flow Rates at Boundary of Subdomain Located in Middle Aquifer Layer Computed by Postprocessor to Exact Values when $\rho_K=3.0$

		$\Delta x=200$ m		$\Delta x=50$ m	
Flow type	Exact (m^3/day)	Postprocessor (m^3/day)	Error (%)	Postprocessor (m^3/day)	Error (%)
Inflows (m^3/day)					
Horizontal	12,961.8	15,815.2	22.0	13,625.3	5.1
From upper layer	83.4	243.3	191.9	89.4	7.3
From lower layer	771.6	462.6	−40.0	714.8	−7.4
Total	13,816.7	16,521.1	19.6	14,429.6	4.4
Outflows (m^3/day)					
Horizontal	13,160.2	16,061.8	22.0	13,830.9	5.1
To upper layer	406.3	458.9	12.9	410.1	0.9
To lower layer	250.2	0.5	−99.8	188.6	−24.6
Total	13,816.7	16,521.1	19.6	14,429.6	4.4
Mass balance error (%)	0.0	0.0	n/a[a]	0.0	n/a

[a]n/a=not applicable.

was used. This led to a total of 1,683 nodes (561 nodes in each layer) and 1,500 elements (500 elements in each layer). Individual elements of each aquifer layer were then assigned a realization of the random K field with $\rho_K=3.0$. Boundary conditions were the same for each layer; i.e., $H_1=200$ m, $H_2=150$ m, and no flow boundary conditions at the south and north sides of the layers (Fig. 3). The exact flow rates were again approximated using MODFLOW (McDonald and Harbaugh 1988) at 6.25 m finite-difference grid resolution.

For this problem, the subdomain depicted as the black region in Fig. 3(b) was defined for each layer in the vertical direction. With this setting, each subdomain received vertical flows as well as horizontal flows. Similar to one- and two-dimensional problems, the finite-element grid was refined progressively to analyze the accuracy of the proposed postprocessor. As an example, Table 3 shows a comparison of simulated flow rates for the subdomain located in the middle layer computed at 200 and 50 m grid resolutions to the exact values. The total simulated inflows are equal to the total simulated outflows demonstrating that the proposed postprocessor also conserves mass in three-dimensional flow fields. The decrease in the errors (%) [see Error (%) columns in Table 3] when the grid spacing is refined is consistent with the findings of the one- and two-dimensional test problems: the accuracy of the flow rates can be increased by refining the grid resolution.

Conclusion

In this paper a postprocessing method to recover the flow rates at element faces based on the groundwater head field computed by the GFEM has been developed and its accuracy has been tested for a set of problems. The test problems included a one-dimensional unsteady flow system in homogeneous aquifer conditions, and one-, two-, and three-dimensional steady flow systems with varying levels of aquifer heterogeneity. The proposed postprocessor is applicable as long as the flow is irrotational. It utilizes the expression for flow that is consistent with the GFEM leading to flow rates that produce precise mass balance locally, as well as globally, at all levels of aquifer heterogeneity and grid resolution. The order of accuracy of the new postprocessor has been shown to be around 1.4. With the flow rates correctly computed at each element face, the new postprocessor allows the mass balance checks at subdomain level as well as at the entire domain. With the proposed method, modelers can quantify the flow rates between adjacent subdomains and study the effect of water management strategies utilized in an individual subdomain on the adjacent subdomains, all in the context of GFEM.

Notation

The following symbols are used in this paper:

f = general source/sink term;
h_i = groundwater head at node i;
K = hydraulic conductivity;
$L_{i,k}$ = length of element face k at node i;
$\mathbf{n}$ = unit outward vector that is perpendicular to boundary;
$\mathbf{n_T}$ = unit tangent at boundary in counterclockwise direction;
Q_i^e = net flow that crosses boundary of patch i in element e;
Q_i^* = circulation at node i;
$\mathbf{q}$ = depth-integrated flux vector;
$\mathbf{q}^*$ = vector that is equal in magnitude to that of depth-integrated flux vector and perpendicular in direction;
S = storativity;
T = aquifer transmissivity;
Γ = boundary that surrounds problem domain;
θ = normal flux at boundary;
ξ_k = length of patch boundary that crosses element face k perpendicularly;
Ω = arbitrary domain over which groundwater conservation equation is expressed weakly; and
ω_i = basis function at node i.

References

Allen, M. B., Herrera, I., and Pinder, G. F. (1988). *Numerical modeling in science and engineering*, Wiley, New York.

Bear, J. (1988). *Dynamics of fluids in porous media*, Dover, New York.

Berger, R. C., and Howington, S. E. (2002). "Discrete fluxes and mass balance in finite elements." *J. Hydraul. Eng.*, 128(1), 87–92.

California Department of Water Resources (CADWR). (2005). *Integrated water flow model (IWFM v 2.3): Theoretical documentation*, Hydrology Development Unit, Modeling Support Branch, Bay-Delta Office, Sacramento, Calif.

Carey, G. F. (1982). "Derivative calculation from finite element solutions." *Comput. Methods Appl. Mech. Eng.*, 35, 1–14.

Carey, G. F. (2002). "Some further properties of the superconvergent flux projection." *Commun. Numer. Methods Eng.*, 18, 241–250.

Carey, G. F., Chow, S. S., and Seager, M. K. (1985). "Approximate boundary-flux calculations." *Comput. Methods Appl. Mech. Eng.*, 50, 107–120.

Chou, S. H., He, S., and Lin, W. W. (2004). "Conservative flux recovery from Q1 conforming finite element method on quadrilateral grids." *Numer. Methods Partial Differ. Equ.*, 20(1), 104–127.

Cordes, C., and Kinzelbach, W. (1992). "Continuous groundwater velocity fields and path lines in linear, bilinear and trilinear finite elements." *Water Resour. Res.*, 28(11), 2903–2911.

Durlofsky, L. J. (1994). "Accuracy of mixed and control volume finite element approximations to Darcy velocity and related quantities." *Water Resour. Res.*, 30(4), 965–973.

Hughes, T. J. R., Engel, G., Mazzei, L., and Larson, M. G. (2000). "The continuous Galerkin method is locally conservative." *J. Comput. Phys.*, 163(2), 467–488.

Lynch, D. R. (1984). "Mass conservation in finite element groundwater models." *Adv. Water Resour.*, 7(2), 67–75.

McDonald, M. G., and Harbaugh, A. W. (1988). "A moduler three-dimensional finite-difference ground-water flow model." *U.S. Geological Survey techniques of water resources investigations*, Book 6, Chap. A1.

Theis, C. V. (1935). "The relationship between the lowering of the piezometric surface and the rate and duration of discharge of a well using groundwater storage." *Trans., Am. Geophys. Union*, 16, 519–524.

Yeh, G. T. (1981). "On the computation of Darcian velocity and mass balance in the finite element modeling of groundwater flow." *Water Resour. Res.*, 17(5), 1529–1534.